Dimerization and dynamics of angiotensin-I converting enzyme revealed by cryoEM and MD simulations

Jordan M. Mancl[1], Xiaoyang Wu[1], Minglei Zhao[2], Wei-Jen Tang[1]

1. Ben-May Department for Cancer Research, The University of Chicago, Chicago, Illinois, United States

2. Department of Biochemistry and Molecular Biology, The University of Chicago, Illinois, United States

Keywords: Angiotensin-I converting enzyme, hypertension, amyloid peptide, cryoEM, all-atom MD simulations.

Author contributions: J.M.M. and W.-J.T., designed the project. X. W. transduced and selected ACE-expression HEK293F cells. J.M.M. and W.-J. T. performed the expression and purification of ACE. J.M.M. performed cryoEM grid preparation, data acquisition and processing assisted by M.Z. and overseen by W.-J. T., and M. Z. J.M.M. built and refined cryoEM structural models and performed heterogeneity analysis. J.M.M. and W.-J. T. performed all-atom MD simulations and analysis. J.M.M. and W.-J.T. wrote the manuscript and all authors contributed to manuscript finalization.

Acknowledgement: We are grateful to Mahira Aragon for grid preparation using Chameleon, Kasahun Neselu for data collection, and Marc Auréle Gilles for assistance with RECOVAR analysis. This work was supported by the NIH grant GM121964 to W.-J. Tang. Some of this work was performed at the National Center for CryoEM Access and Training (NCCAT) and the Simons Electron Microscopy Center located at the New York Structural Biology Center, supported by the NIH Common Fund Transformative High Resolution Cryo-Electron Microscopy program (U24 GM129539,) and by grants from the Simons Foundation (SF349247) and NY State Assembly.

Abstract (175 words)

Angiotensin-I converting enzyme (ACE) regulates the levels of disparate bioactive peptides, notably converting angiotensin-I to angiotensin-II and degrading amyloid beta. ACE is a heavily glycosylated dimer, containing 4 analogous catalytic sites, and exists in membrane bound and soluble (sACE) forms. ACE inhibition is a frontline, FDA-approved, therapy for cardiovascular diseases yet is associated with significant side effects, including higher rates of lung cancer. To date, structural studies have been confined to individual domains or partially denatured cryoEM structures. Here we report the cryoEM structure of the full-length, glycosylated, sACE dimer. We resolved four structural states at 2.99 to 3.65 Å resolution which are primarily differentiated by varying degrees of solvent accessibility to the active sites and reveal the full dimerization interface. We also employed all-atom molecular dynamics (MD) simulations and heterogeneity analysis in cryoSPARC, cryoDRGN, and RECOVAR to elucidate the conformational dynamics of sACE and identify key regions mediating conformational change. We identify differences in the mechanisms governing the conformational dynamics of individual domains that have implications for the design of domain-specific sACE modulators.

Introduction

Angiotensin-I converting enzyme (ACE) is an M2 clan zinc metalloprotease (EC3.4.15.1) located on the plasma membrane and in the extracellular milieu (Bernstein *et al*, 2013; Lubbe *et al*, 2020; Turner & Hooper, 2002). ACE plays a crucial role in the renin-angiotensin system by converting angiotensin I to the potent vasoconstrictor angiotensin II, and in the kinin-kallikrein system by degrading bradykinin, a potent vasodilator. Inhibiting ACE is a primary approach for treating hypertension and is a proven therapy for heart failure, diabetic nephropathy, and other cardiovascular and renal dysfunctions (Herman *et al*, 2024). However, ACE inhibition has known side effects, e.g., dry cough and angioedema, and has been linked to higher rates of lung cancer (Wu *et al*., 2023). This is partly because ACE also degrades a diverse range of peptides, resulting in complex physiological outcomes due to the interplay in altering levels of these peptides (Bernstein *et al*, 2018; Danziger *et al*, 2023; Herman *et al.*, 2024; Semis *et al*, 2019; Zheng *et al*, 2022). Furthermore, ACE degrades amyloid β (Aβ), which is associated with the progression of Alzheimer's diseases (Hampel *et al*, 2021; Hemming & Selkoe, 2005; Zhang *et al*, 2023; Zou *et al*, 2009). Overexpression of ACE in myelomonocytes substantially reduced Aβ load and prevented Alzheimer's disease-like cognitive decline in mice (Bernstein *et al*, 2014). However, the brains of some Alzheimer's disease patients showed upregulation of the renin-angiotensin system which led to deleterious effects and ACE inhibition was beneficial (Gouveia *et al*, 2022; Qiu *et al*, 2013; Wright *et al*, 2013). These studies indicate that global ACE inhibition could be either beneficial or harmful for individual Alzheimer's patients, and underscores a need for better understanding the molecular mechanisms governing ACE function and substrate selectivity to develop more selective, improved, ACE inhibitors and expand ACE-based therapies (Gouveia *et al.*, 2022; Qiu *et al.*, 2013; Wright *et al.*, 2013).

ACE is a 180 kDa heavily N-linked glycosylated type 1 transmembrane protein with two homologous catalytic domains residing at the N- and C-terminal ends (ACE-N and ACE-C) in its extracellular region (Bernstein *et al.*, 2013; Riordan, 2003; Turner & Hooper, 2002). The ACE extracellular region can be released via proteolytic cleavage near the transmembrane region by ADAM family protease(s), generating soluble ACE (sACE) (English *et al*, 2012). ACE belongs to the cowrin (cowry like) family of zinc metallocarboxypeptidases because its catalytic domain is ellipsoidal and contains a long,

deep, yet narrow catalytic cleft (Gomis-Ruth, 2008). ACE is known to cleave short peptides, such as angiotensin I (decapeptide) and bradykinin (nonapeptide) by removing the C-terminal two amino acid residues. Different from the funnelin family of metallocarboxypeptides that contains a funnel-like cavity, the catalytic cleft of ACE can accommodate entire oligopeptides and ACE has been shown to cleave multiple discrete sites on Aβ outside the C-terminal end (Zhou et al., 2009). Thus, it is more accurate to refer to ACE as an endopeptidase with dipeptidyl carboxylase activity.

Extensive crystallographic studies of ACE-N or ACE-C alone and in complex with various inhibitors and a catalytic product, angiotensin-II, have elucidated the overall structures of ACE catalytic domains and molecular details of the catalytic pockets (Acharya *et at.,* 2024; Corradi *et al.,* 2006; Lubbe *et al.,* 2020; Masuyer *et al.,* 2012; Natesh *et al.,* 2003b). The structures indicate that each domain is comprised of three sub-domains and offer insight for the substrate preferences around cleavage sites and the promiscuity of each domain toward short peptide substrates. Furthermore, they reveal the orientation of substrate binding sites around scissile bond, indicating that the entire oligopeptide substrates need to be engulfed into the catalytic chamber of ACE catalytic domain (Acharya *et al.,* 2024; Masuyer *et al.,* 2012; Natesh *et al.,* 2003a).

However, the catalytic pocket of ACE in the closed state is not large enough to accommodate the entrance of all its known substrates, particularly Aβ, to permit the observed cleavage pattern. Thus, similar to other Aβ-degrading proteases, such as insulin degrading enzyme (IDE), presequence protease (PreP), and neprilysin (NEP), ACE must undergo a large-scale open-closed transition to capture and degrade larger peptide substrates such as Aβ (Liang *et al.,* 2022; Malito *et al.,* 2008; Zhang *et al.,* 2018). Recent open state structures of sACE-N, sACE monomer, and a sACE-N dimer, along with molecular dynamics (MD) simulations of sACE-C, have begun to reveal the conformational heterogeneity, though it remains under-studied (Cozier *et al*, 2021; Lubbe *et al*, 2022; Phan *et al*, 2020).

The extracellular domains of ACE are readily dimerized in the membrane-bound and soluble forms. Both the ACE-N and ACE-C domains within the ACE monomer are catalytically active and each has its own substrate preferences (Bernstein *et al.,* 2011; Semis *et al.,* 2019; Zou *et al.,* 2009). For example, ACE-N can convert Aβ1-42 to Aβ1-40,

105 which is less amyloid fibril-prone than Aβ1-42 but ACE-C cannot (Zou *et al.*, 2009).
106 Accumulating evidence support a complicated interplay between ACE-N and ACE-C
107 within the ACE dimer. Enzyme kinetics analysis suggests negative cooperativity between
108 two catalytic domains (Binevski *et al*, 2003; Rice *et al*, 2004; Skirgello *et al*, 2005).
109 However, ACE also exhibits positive synergy toward Aβ cleavage and allostery to
110 enhance the activity of its binding partner, bradykinin receptor (Erdos *et al*, 2010; Zou *et*
111 *al.*, 2009). Recently, cryoEM structures of soluble dimeric apo-sACE were reported
112 (Lubbe *et al.*, 2022); however, due to the poor resolution/denaturation of sACE-C, only
113 full-length ACE monomer or dimeric sACE-N was reported. Here, we present four discrete
114 cryoEM structures of full-length sACE that contain all four catalytic domains (Fig. 1A).
115 This is followed by cryoEM heterogeneity analysis and all-atom MD simulations. Together,
116 our analyses provide structural insights into domain interactions, open-closed transitions
117 of the catalytic domain, and conformational dynamics of soluble dimeric ACE.

118 **Results**

119 **Structures of the full-length sACE dimer determined by single particle cryoEM**

120 Soluble human ACE (sACE), which includes the entire extracellular region of ACE,
121 was expressed in HEK293F cells and purified from culture supernatant using an ion
122 exchanger (Source Q) followed by size exclusion chromatography (Superdex S200).
123 Buffer conditions suitable for single particle cryoEM analysis were identified and
124 optimized using differential scanning fluorometry (Figure S1). Purified sACE was then
125 vitrified using a Vitrobot, and a dataset of ~3,600 micrographs was collected on a 300
126 keV Titan Krios equipped with a Gatan K3 camera at the University of Chicago Advanced
127 Electron Microscopy Facility (Table S1). The data was processed in cryoSPARC v4.4.0
128 (Figure S2). After filtering ~1.1 million picked particles to ~378K using 2D and 3D
129 classification, three classes were identified (Figure 1, Figure S2). Of these, ~268K
130 particles mapped to a dominant 2-domain class reconstructed as an ACE-N dimer, while
131 ~21K particles mapped to a minor 3-domain class containing two ACE-N and only one
132 ACE-C, reminiscent of the recently published ACE cryoEM structure (Lubbe *et al.*, 2022).
133 The remaining 89K particles mapped to a full-length ACE dimer containing two ACE-N
134 and two ACE-C, which was refined to 3.65Å resolution (Figure 1C, S2, Movie S1, Table
135 S1).

The partial denaturation of macromolecules during vitrification has been attributed mainly to repeated exposure of the macromolecules to the air-water interface (Glaeser, 2018; Noble *et al*, 2018). The sACE-C domain was shown to be less stable than the ACE-N domain (Voronov *et al.,* 2002), so we hypothesized that repeated exposure to the air-water interface could cause preferential denaturation of ACE-C. We have previously showed that preferential denaturation of human PreP occurred in one of its two homologous domains and that faster vitrification using Chameleon significantly prevented such preferential denaturation (Liang *et al*, 2022). Therefore, we collaborated with the National Center for CryoEM Access and Training (NCCAT) to prepare sACE grids using Chameleon (Darrow *et al*, 2019). Chameleon preparation reduced the time the sample spends on the grid before freezing by more than 10-fold. We collected a new dataset of ~18,000 micrographs and our 2D classification revealed a higher percentage of particles for four-domain classes than those prepared using the Vitrobot (Figure 1B). However, our 3D classification still showed the existence of structures of the ACE-N only dimer and those containing two ACE-N and one ACE-C (Figure S3). This indicates that the reduction in vitrification time using Chameleon reduced but did not prevent preferential denaturation.

From these data, we obtained a map for a consensus ACE structure that achieved a resolution of 2.8Å. However, while the core region showed excellent map quality, the map quality for the dynamic regions corresponding to the open-close transition of ACE catalytic domains was poor, suggesting multiple discrete conformational states exist. We thus performed 3D classification and reconstructed three distinct conformational states of full-length apo-ACE at resolutions of 2.99Å, 3.05Å, and 3.15Å (Figure 1C, S3, Movie S2-4, Table S1). We refer to these ACE dimer structures by their resolutions, namely ACE-2.99, ACE-3.05, and ACE-3.15, along with the structure from data obtained using the Vitrobot, ACE-3.65. Given the rich structural information from more than 50 reported crystal structures of ACE and one recently reported cryoEM study of ACE, below we focus on the new insights that our ACE dimer structures offer (Acharya *et al*, 2024; Corradi *et al*, 2006; Lubbe *et al.*, 2020; Lubbe *et al.*, 2022; Masuyer *et al*, 2012; Natesh *et al*, 2003).

The overall structures of sACE dimers and structural insight into dimerization

Soluble ACE has two homologous catalytic domains: ACE-N (amino acids 31-644) and ACE-C (amino acids 645-1231). Based on the comparison of various catalytic

168 domains of our ACE dimer structures, we subdivide each catalytic domain of ACE into
169 three subdomains: D1a, D1b, and D2 for ACE-N, and D3a, D3b, and D4 for ACE-C
170 (Figure 1A). These three subdomains in either ACE-N or ACE-C form a catalytic chamber.
171 The catalytic zinc ion is coordinated by the canonical HEXXH motif residing in the D1b
172 and D3b subdomains (Figure 1A). Four sACE dimer structures manifest as pseudo-
173 symmetric C2 homodimers across the dimer interface. The dominant symmetry-breaking
174 features are the degrees of displacement between D1 and D2 or between D3 and D4,
175 leading to changes in solvent accessibility to the catalytic pockets.

176 Based on the openness of the catalytic chamber, defined at the distance between
177 the D1/3a and D2/4 helices that gate access, we classified sACE-N into three
178 conformational states: open (O), intermediate open (I), and closed (C) (Figure 2A); sACE-
179 C is significantly less open than sACE-N in our structures, and is only classified into
180 intermediate (I) and closed (C) states (Figure 2B). The four sACE dimer structures differ
181 mostly by the degrees of openness of their four catalytic domains (Figure 2C, D). Our
182 sACE-2.99 and sACE-3.65 structures are globally similar, both contain sACE-N domains
183 in the open and intermediate states and sACE-C domains in the closed and intermediate
184 states. In sACE-3.05, both sACE-N domains adopt an open state, while the sACE-C
185 domains adopt an intermediate and closed state. In the sACE-3.15 structure, one subunit
186 has both sACE-N and sACE-C adopting a closed conformation, while the other subunit
187 has an open sACE-N domain and an intermediate sACE-C domain.

188 Our four cryoEM structures of sACE provide the structural basis for sACE
189 dimerization. sACE dimerization is mediated by interfaces between D2 subdomains and
190 D4 subdomains of sACE monomers. The D2 and D4 subdomains generally have much
191 lower B-factors than the D1 and D3 subdomains (Figure S4). The interaction of the D4-
192 D4 subdomains is analogous to the D2-D2 interaction, yielding an RMSD of ~1 Å² when
193 aligned (Figure 3A). The primary source of variation is a general rigid body shift away
194 from the interaction interface for non-interacting regions in the D4-D4 region compared to
195 the D2-D2 region. The observed D2-D2 interface is consistent with one of three possible
196 contacts between sACE-N in the non-crystallographic symmetry mates from previous
197 crystallographic analysis of sACE-N and the previously published cryoEM structure
198 (Figure S5). In total, the interface between sACE monomers buries a surface area of
199 approximately 1,900 Å². Although sACE-N and sACE-C are structurally analogous, their

respective interfaces (sACE-N/N and sACE-C/C) are not equivalent. The sACE-N/N interface is larger and stronger, burying a surface area of approximately 1,150 Å², compared to a buried surface area of approximately 750 Å² for the sACE-C/C interface.

The interface between sACE-N is formed by a hydrophobic core, anchored by a Y494 π-stacking interaction, and flanked by salt bridges formed by R482 and R487 as well as E241 and E248 along with a collection of polar and van der Waal contacts (Figure 3B). The dimer interface between two sACE-N domains is completed by glycan-glycan interactions between the glycans attached to N111, which is consistent with the role of glycosylation in sACE dimerization (Figure 3C) (Kost *et al*, 2000). However, the central residues that form the hydrophobic core of the interface between sACE-N are not present in the interface between sACE-C. Instead, the sACE-C interface is formed by a symmetric salt bridge between K1096 and E1089, side chain-backbone interactions, and van der Waals contacts (Figure 3D).

Conformational states of sACE catalytic domains

The comparison of our dimeric sACE cryoEM structures of reveals the conformational dynamics of sACE catalytic domains. The four sACE dimer structures represent different combinations of open, intermediate, and closed states of ACE catalytic domains (Figure 2). By aligning each sACE-N and sACE-C region in our structures to the D2/4 domain, it becomes clear that our structures represent a continuous gradient of structural heterogeneity, ranging from the most closed state to the most open state (Figure S6).

The comparison of sACE-N in its open and closed states reveals the structural basis for the open-to-closed transition of this domain. Our structures show that when the tip connecting the two long helices of the D1a subdomain moves away from the D2 subdomain, resulting in the open state, the opposite end of the helix moves closer to the D2 subdomain, as if the helix were balanced upon a fulcrum (Figure 4A, B). Detailed structural analysis indicates that the fulcrum is primarily formed by the salt bridge between two highly conserved residues: E95 in the D1a subdomain and R137 in the D2 subdomain. To stabilize the open state, additional salt bridges are formed, with D218 in the D2 subdomain pairing with K102 in all cases and occasionally with R125 in the D1a subdomain (Figure 4A). The loss of this salt bridge in the closed state is compensated for

231 by the formation of a network of van der Waals interactions between the D1a and D2
232 subdomains that stabilize the closed state. The transition between open and closed states
233 is likely influenced by the binding of substrates and reaction products during the ACE
234 catalytic cycle. Although a similar fulcrum mechanism is not evident in the sACE-C
235 domain, the connection between the D3a and D2 subdomains would act as a lever to
236 pivot sACE-C from the closed to the open state. The closed state of sACE-C is also
237 stabilized by a network of van der Waals contacts between the D3a and D4 subdomains.

238 On average, sACE-N is more open than sACE-C, likely due to multiple factors
239 (Figure 2D). In sACE-N, the D1a subdomain is at the N-terminal end of sACE, allowing
240 for a greater range of motion (Figure 4B), while the fulcrum and stabilization mechanisms
241 can maintain sACE-N in a more widely open state (Figure 4A). Conversely, in sACE-C,
242 the motion of the D3a subdomain is constrained by its connection to the D2 subdomain
243 (Figure 4C). Additionally, there are sequence differences at the interface between the
244 three subdomains of sACE-N and sACE-C. In the most closed state—the B chain sACE-
245 C domain of the sACE-3.05 structure—residues from all three subdomains, including
246 I678, V753, V955, and V956, form a hydrophobic latch that stabilizes the closed state
247 (Figure 4D). The hydrophobic latch in sACE-N is weaker because the residue
248 corresponding to V753 has been replaced with a threonine (Figure 4D).

249 We performed a series of all-atom molecular dynamics (MD) simulations to explore
250 the conformational dynamics of sACE. A total of 8 apo-sACE simulations were conducted,
251 comprising four simulations with non-glycosylated sACE (>1.8 μs each) and four with
252 sACE where all 12 N-linked glycosylation sites have complex glycans (>2 μs each) (Movie
253 S5, S6). Glycan orientations were randomized prior to each simulation to avoid bias. We
254 did not observe a substantial difference in the global conformational dynamics between
255 our sets of simulations with and without glycans. The domain motions of these simulations
256 are summarized in Table S2. Below, we focus on the general features from these
257 simulations.

258 RMSD analysis reveals that the dominant source of conformational change in our
259 simulations is the open-close transition between the D1/3 and D2/4 domains (Figure S7).
260 The D2/D2 and D4/D4 regions are the most stable, with the bulk of conformational
261 changes localized to the D1/D3 domain. Within the D1/3 domain, we observed that the
262 D1/3a motion was not always correlated with D1/3b or D2/D4, meaning that at a given

263 time, D1/3a could move along with D1/3b, or with D2/D4, or independently. Consistent
264 with our structural analysis, our MD simulations also indicate that sACE-N displays a
265 much wider range of opening geometries than sACE-C. Most of our MD simulations
266 rapidly closed, preventing an effective comparison of the open vs closed state dynamics.
267 However, the slowest closing simulation did reveal a correlation with our previously
268 described “fulcrum” mechanism of opening for sACE-N (Figure 4A). Our simulation
269 revealed that the K102-D215 interaction was maintained for the entire time that sACE-N
270 adopted an open conformation, yet this interaction was lost when sACE-N transitioned to
271 the closed state (Figure 4E).

272 The MD simulation of glycosylated ACE provides additional structural insights into
273 the structure and functions of N-linked glycosylation of ACE. Glycosylation is shown to
274 affect the folding, secretion, and stability of ACE (O'Neill *et al*, 2008; Sadhukhan & Sen,
275 1996). Our MD simulation reveals that the dynamics of 12 N-linked glycans cover a large
276 surface area of ACE, shielding it from environmental insults (Figure S8). Consistent with
277 observations from our Coulomb potential density maps and previously published data, we
278 observed a substantial and persistent inter-subunit interaction between glycans from
279 N111 (Figure 3C). From room mean square fluctuation (RMSF) analysis, glycosylation
280 was found to increase the overall dynamicism of sACE (Figure S9). Furthermore, while
281 there are N-linked glycans near the catalytic chamber, particularly those at the tip of D1a
282 and D3a, they were highly dynamic and did not occlude access to the catalytic chamber.
283 This is consistent with the observation that deglycosylation only modestly increases the
284 enzymatic activity of ACE (Baudin *et al*, 1997; Orth *et al*, 1998; Yu *et al*, 1997).

285 We also performed three simulations on the non-glycosylated sACE monomer (>1
286 microsecond each) (Table S2). We observed the expected intra-subdomain open-closed
287 motions in sACE-N and sACE-C that were also observed in the simulations of ACE dimer.
288 We also observed that the motion of sACE-C relative to sACE-N was significantly greater
289 in our monomer simulations compared to our dimer simulations. This suggests that
290 dimerization places significant constraints upon the conformational dynamics of sACE.
291 Previous work has defined the conformational dynamics of sACE from cryoEM data
292 where both sACE-C domains were not resolved. Given our observations from the
293 monomeric and dimeric MD simulations, we endeavored to understand the

294 conformational heterogeneity present within our cryoEM data to better understand the
295 impact of dimerization on sACE dynamics.

296 **CryoEM heterogeneity analysis of sACE**

297 CryoEM structures are ensemble averages of many aligned particle images.
298 Recently, there have been many approaches developed to understand the particle
299 heterogeneity present within a cryoEM structure as a proxy for molecular motion (Tang *et*
300 *al*, 2023). We employed three methods of heterogeneity analysis: cryoDRGN, RECOVAR,
301 and 3D Variability Analysis (3DVA) (Punjani & Fleet, 2021; Zhong *et al*., 2021; Gilles &
302 Singer 2024). CryoDRGN employs neural networks to resolve structural heterogeneity in
303 a nonlinear, multidimensional latent space, while RECOVAR and 3DVA both employ linear
304 subspace methods. 3DVA finds the linear subspace by an alternating optimization
305 scheme to capture image variations while RECOVAR utilizes a regularized covariance
306 estimator to identify subspaces that best capture the distribution of states.

307 We conducted this analysis on both of our datasets and found the results to agree,
308 therefore, we focus on the larger, and higher-resolution dataset collected at NCCAT
309 below. For analysis, the entire particle set, prior to 3D classification and consisting of
310 ~170k particles, was utilized. The particle alignments from the same C1 consensus
311 refinement were used as input for each of the three methods as current methods to
312 investigate particle heterogeneity are highly dependent upon initial pose assignment of
313 individual particles. Globally, all three methods agreed with our ensemble structures, in
314 that the dominant source of structural variability within our particle population could be
315 described by the open-closed transition of individual domains, and that sACE-N displayed
316 more variability than sACE-C.

317 Initially, we performed 3D variability analysis (3DVA) in cryoSPARC to provide a
318 direct comparison to the previously published analysis of the partial ACE cryoEM structure
319 (Punjani & Fleet, 2021) (Figure 5A). Trajectories were reconstructed along the top 5
320 principal components of variance (Movie S7). Surprisingly, the trajectory describing the
321 variance along the first principal component vector suggests a dominant inter-domain
322 motion, where the sACE-N/N region bends towards the sACE-C/C region. The trajectories
323 along the remaining principal component vectors comprise varying combinations of
324 individual domains undergoing the open-close transition. Consistent with our previous

325 observations, the range of presumptive motion in these trajectories is greater in sACE-N
326 than sACE-C. Previous 3DVA performed on the ACE monomer structure revealed 4 types
327 of potential motion, termed bending, pivoting, breathing, and jumping (Lubbe *et al.*, 2022).
328 The breathing motion matches the open-close transition that dominates most of our
329 principal component vectors, while the bending motion appears to correlate with the
330 variance described by our top principal component vector. We did not observe any
331 potential motions reminiscent of the jumping or pivoting motions in our 3DVA.
332 Furthermore, the magnitude of the bending motion in our 3DVA is substantially less than
333 previously reported for the partial ACE structure. Together, this highlights a significant
334 difference in the conformational dynamics between ACE dimer and monomer and
335 suggests dimerization functions as a key constraint to the conformational dynamics of
336 sACE.

337 We then moved on to analyze our data using cryoDRGN, which revealed that the
338 data formed a single cluster across multiple dimensions (Figure 5B, S10). Trajectories
339 generated along five principal component vectors of structural variance were dominated
340 by the open-close transition, primarily in sACE-N (Movie S8). We observed little variance
341 in sACE-C and, unlike 3DVA, cryoDRGN did not reveal any substantial inter-domain
342 motions. Faced with this discrepancy between the 3DVA and cryoDRGN results, we
343 employed a third method, RECOVAR, to further analyze our data. Similar to cryoDRGN,
344 RECOVAR revealed that our data formed a singular cluster across multiple dimensions
345 of analysis. Volumes representative of kmeans cluster reconstructions were similarly
346 consistent with our cryoDRGN results. RECOVAR indicated that the primary source of
347 structural variance could be explained by the open-close transition, primarily of the sACE-
348 N domains. With this in mind, we repeated the RECOVAR analysis with a focus mask
349 around the sACE-N/N region. We then estimated the conformational density by
350 deconvoluting the multidimensional latent space with a two-dimensional principal
351 component analysis. The resulting density plot revealed four clusters which corresponded
352 to different conformations of the sACE-N/N region (Figure 5C). The most populous cluster
353 corresponded to a state where both sACE-N subunits adopted an open conformation.
354 The second largest cluster, and the smallest cluster, corresponded to a state where one
355 sACE-N was open and the other was closed. The discrepancy in population size between
356 these clusters is likely due to bias in the initial particle poses, rather than a subunit-specific

357 preference for the open state. The final cluster corresponded to a state where both sACE-
358 N subunits adopted the closed conformation. We then used RECOVAR to generate a
359 trajectory through the latent space to predict a potential transition pathway from the
360 closed-closed state to the open-open state (Movie S9). This trajectory revealed that one
361 subunit would open, followed by the second, and raised the question of potential allostery
362 or coordinated motion between the adjacent sACE-N domains. 3DVA, cryoDRGN, and
363 RECOVAR all appeared to display varying degrees of coordinated motion between sACE
364 domains, yet this type of analysis lacks an explicit time component, so it is not possible
365 to draw concrete conclusions regarding coordinated motion. Likewise, while MD
366 simulations contain an explicit time factor, most of our MD simulations closed quickly, and
367 did not reopen. Thus, while we did not observe coordinated motion from our simulations,
368 no conclusion can be reached because of limited intradomain motions. To investigate
369 coordination between the sACE-N domains, we performed 3D classification in
370 cryoSPARC with a focus mask on a single sACE-N domain and requested 2 classes
371 (Figure 5D). The particles were split roughly evenly between the two classes, one
372 resulting in an open state and the other being closed. We then used these classes for
373 another round of 3D classification with a focus mask on the opposite sACE-N domain and
374 again asked for 2 classes. Again, these particles were split roughly evenly among the
375 classes, leaving us with four similarly sized classes adopting the same conformations as
376 the clusters revealed by RECOVAR. As a result, we are unable to find any evidence of
377 coordinated motion between sACE-N domains in the absence of substrate.

378 **Discussion**

379 Our cryoEM and MD simulations analysis of the extracellular regions of dimeric
380 ACE offers insights into the stability of ACE catalytic domains. We show that ACE dimer
381 interface consists of three major components, protein-protein interfaces between ACE-N,
382 glycan-glycan interaction between ACE-N, and protein-protein interface between ACE-C.
383 The interface between ACE-N, in general, is 50% larger and has higher numbers of
384 hydrogen bonds and salt bridges than that between ACE-C. The necessity for the stronger
385 interaction between ACE-N is likely due to that ACE-N is distal to transmembrane helix
386 so that the additional reinforcement is required. The weaker interaction and lack in the
387 contribution from glycan in the interface between ACE-C could also explain the observed
388 preferential denaturation of ACE-C despite the high structural similarity between ACE-N

389 and ACE-C. The denaturation is likely due to the exposure to air-water interface during
390 vitrification, a common issue in single particle cryoEM analysis (Glaeser, 2018; Noble *et*
391 *al.*, 2018). We have partially overcome the denaturation issue of ACE-C by optimizing the
392 buffer pH to increase the melting temperature and using the faster plunging time during
393 vitrification afforded by Chameleon to reduce the exposure to air-water interface (Figure
394 1). However, we did not completely prevent the preferential denature of ACE-C during
395 vitrification.

396 ACE is part of a family of proteases capable of effectively degrading Aβ. This family
397 includes M16 metalloproteases like IDE and PreP, and M13 metalloproteases such as
398 neprilysin and endothelin converting enzyme. Integrative structural analysis has
399 demonstrated how IDE employs conformational dynamics, charge, and secondary
400 structure complementarity to selectively capture peptide substrates into its sizable
401 catalytic chamber, subsequently unfolding and degrading amyloidogenic peptides such
402 as insulin and Aβ, without degrading structurally similar yet non-amyloidogenic peptides
403 (Malito *et al*, 2008; Tang, 2016; Zhang *et al*, 2018). The other mentioned enzymes also
404 belong to this group of chamber-containing proteases, known as cryptidases (Liang *et al*,
405 2021; Liang *et al.*, 2022; Malito *et al.*, 2008). Similar to cryptidases, structural analysis
406 reveals that ACE must undergo an open-closed transition to capture, engulf, and degrade
407 its oligopeptide substrates, such as angiotensin 1 and bradykinin.

408 Our apo-ACE structures and MD simulations identify a fulcrum mechanism that
409 governs the open-closed transition of ACE-N, while the interplay between ACE-N and the
410 D3a domain likely plays a crucial role in this transition. Analogous to the binding of MB60,
411 a PreP inhibitor, to the hydrophobic pocket to trigger the open to closed transition, factors
412 such as binding of substrates and ACE inhibitors may alter the balance, leading to the
413 regulation of ACE activity (Liang *et al.*, 2022). We also observe that the catalytic pocket
414 of the ACE catalytic domain is not large enough to engulf the entire Aβ. Additionally, the
415 distances between the domains (ACE-N to ACE-C, ACE-N to ACE-N, or ACE-C to ACE-
416 C) are too large for these domains to bind Aβ simultaneously (Chen *et al*, 2017).
417 Therefore, ACE likely employs a different mechanism from IDE and PreP to selectively
418 bind and degrade Aβ. Future integrative structural studies await to reveal how ACE
419 selectively recognizes and degrades a diverse array of substrates.

420 Single particle cryoEM holds significant promise for revealing the conformational
421 dynamics of biological macromolecules from embedded heterogeneity. Consequently,
422 cryoEM heterogeneity analysis is an active and rapidly evolving field providing insights
423 into the conformational dynamics and allostery of macromolecules (Tang *et al.*, 2023).
424 However, many challenges exist in using cryoEM heterogeneity analysis due, in part, to
425 the low signal-to-noise ratio in observed micrographs. Often, these analyses address
426 questions difficult or impossible to tackle experimentally, leaving no ground truth for
427 validation. We encounter such challenges in our heterogeneity analysis as well.
428 Consistent with our single particle cryoEM structural analysis, we observed the expected
429 intradomain open-closed transition using cryoDRGN, cryoSPARC 3DVA, RECOVAR, and
430 all-atom MD simulation. Surprisingly, we did not observe such motion using cryoSPARC
431 3DFlex, a neural network-based method analyzing our cryoEM data of sACE (Punjani &
432 Fleet, 2023). Central to the working of cryoSPARC 3DFlex is the generation of a
433 tetrahedral mesh used to calculate deformations within the particle population. Proper
434 generation of the mesh is critical for obtaining useful results and must often be determined
435 empirically. Despite several attempts, we were unable to obtain mesh conditions suitable
436 to observe any open-close transition, illustrating a limitation of cryoSPARC 3DFlex.

437 The interplay between ACE-N and ACE-C within the ACE dimer has complicated
438 consequences for ACE functions, showing negative cooperativity for enzymatic activities
439 while exhibiting positive synergy in Aβ cleavage by ACE-N and activity at the bradykinin
440 receptor (Binevski *et al.*, 2003; Erdos *et al.*, 2010; Rice *et al.*, 2004; Skirgello *et al.*, 2005;
441 Zou *et al.*, 2009). Understanding the conformational dynamics in both inter- and intra-
442 domain motions of the extracellular regions of the ACE dimer holds promise for designing
443 ACE modulators to improve and broaden the therapeutic use of ACE modulation. Our
444 cryoEM heterogeneity analysis has revealed coordinated open-closed transitions across
445 four catalytic domains using cryoDRGN and cryoSPARC 3DVA, which could potentially
446 provide the molecular basis for ACE allostery (Figure 5A,B, Movies S7,8). However, our
447 RECOVAR analysis reveals independent motion of two ACE-N domains, not the
448 coordinated motion revealed by cryoDRGN and cryoSPARC 3DVA (Figure 5C).
449 Furthermore, our focused classification using cryoSPARC failed to reveal a profound
450 association between specific conformational states of the ACE catalytic domains, an

451 expectation from the trajectories revealed by cryoDRGN and cryoSPARC 3DVA (Figure
452 5D).

453 The first principal component trajectory in our 3DVA analysis revealed a significant
454 potential interdomain motion between sACE-N/N and sACE-C/C, yet cryoDRGN and
455 RECOVAR did not reveal any inferred motions of similar magnitude. Notably, the
456 trajectory revealing this potential interdomain motion in 3DVA was absent any variability
457 in the sACE-N open/close transition. In our study, this conformational heterogeneity
458 appears to stem from subtle yet significant conformational differences between the two
459 chains within an ACE dimer and the inability of cryoSPARC to properly align these
460 conformationally distinct chains (Figure S11). CryoDRGN and RECOVAR revealed
461 smaller magnitudes of potential interdomain motions, which were often accompanied by
462 various combinations of individual domains opening and/or closing. This suggests that
463 the apparent discrepancy in the magnitude of inferred interdomain motion could be a
464 result of the different theoretical approaches of dimensionality reduction and trajectory
465 generation employed by the respective methods of analysis and underscores the
466 importance of incorporating multiple methods of analysis in the absence of a singular
467 "gold-standard" of heterogeneity analysis.

468 Advances in single-particle cryoEM analysis have enabled detailed structural
469 examination of the extracellular domains of the ACE dimer. Beyond its implications for
470 future drug discovery efforts aimed at enhancing ACE-based therapies, ACE can serve
471 as a valuable model of a multi-domain glycoprotein for studying methods to preserve
472 sample integrity, particularly due to the high propensity of ACE-C to denature during
473 vitrification. Furthermore, considering the aforementioned challenges and caveats, we
474 propose that, due to its size, biomedical importance, and the complexity of its motions,
475 ACE also represents an excellent model system for evaluating and improving cryoEM
476 heterogeneity analysis.

477 **Experimental procedures**

478 **Expression of human sACE**: Human 293T and 293F cells were maintained in DMEM +
479 10% fetal calf serum (FCS). The lentiviral plasmid for the expression of the extracellular
480 domain of human ACE (sACE, aa 1-1231) that contains a 6-histidine tag at its C-terminus
481 was made by Vectorbuilder and co-transfected with helper plasmids to human 293T cells

482 for lentiviral production. Human 293F cells were infected with the resulting virus and
483 selected for stable sACE expression. 293F that stably expressed sACE grew poorly in
484 Free-style 293 media (ThermoFisher 12338018). Thus, for ACE production, 293F cells
485 that stably expressed sACE were first grown in DMEM+10% FCS at 37°C and gradually
486 shifted into Free-style 293 media by reducing FCS by first in Free-style 293 media + 2%
487 FCS and then to media without FCS. These cells were then shifted to and maintained in
488 30°C for 3-5 days for ACE production to reduce proteolysis.

489 **Purification of soluble human ACE:** Culture supernatant was centrifuged at 3,000xg for
490 5 min, diluted 10-fold with 25 mM Tris-HCl pH 8, filtered, and run over a Source Q column
491 pre-equilibrated with 25 mM Tris-HCl pH 8. Column was washed to baseline with Tris-HCl
492 pH 8 and bound protein was eluted with a linear gradient of NaCl to 1 M. sACE containing
493 fractions were pooled and EDTA was added to 10 mM to strip the catalytic zinc ion.
494 Sample was concentrated and run over a Superdex S200 SEC column pre-equilibrated
495 with the desired cryoEM buffer.

496 **Differential scanning fluorometry (DSF)**: To optimize the grid making conditions,
497 differential scanning fluorimetry was applied to screen 96 buffers conditions. DSF was
498 performed with 3 mg/ml sACE and 10X Sypro Orange in 20 µl buffers in a Thermo Fisher
499 Step ONE RT-PCR thermocycler. Using the melting temperature and slope as selective
500 criteria, 25 mM citrate pH 5.5, 25 mM sodium phosphate pH 5.5, 150 mM NaCl, 10 mM
501 EDTA was identified as the ideal buffer condition and used for all subsequent cryoEM
502 experiments.

503 **CryoEM data collection and processing:** Peak fractions were collected off the SEC
504 column and used to immediately prepare grids, resulting in a protein concentration of ~4.5
505 mg/ml. Quantifoil R1.2/1.3 Cu200 grids were glow-discharged in air and grids were
506 prepared by Vitrobot mark 3. 3.5 µl of sample was applied to the grid in the chamber with
507 100% humidity, 25°C. Excess sample was blotted for 1 sec, blot force 2, and grids were
508 plunge frozen in liquid ethane. All images were acquired using a Titan Krios microscope
509 (FEI) operated at 300KeV with a Gatan K3 direct electron detector. A dataset of ~3,600
510 micrographs was collected at The University of Chicago Advanced Electron Microscopy
511 facility. The dataset was processed using cryoSPARC (Figure S1) (Punjani *et al*, 2017).
512 Briefly, a four-domain sACE dimer model was generated using sACE-N dimer and sACE
513 monomer and adjusting the distance between ACE-C domains to avoid steric clashes as

514 a template for particle picking (Lubbe *et al.*, 2022). After template picking, 1.1 million
515 particles were extracted with a box size of 360 pixels. Several rounds of 2D classification
516 were used to remove junk particles. ~577K particles were processed in successive rounds
517 of *ab initio* reconstruction and heterogeneous refinement. sACE grids were also prepared
518 using Chameleon and collected a dataset of ~19,000 micrographs at the National Center
519 for CryoEM Access and Training. For those, Quantifoil Active R 1.6/0.9 Cu/Rh 300 were
520 coated with gold using a Safematic CCU-010 Compact Coating Unit. Briefly, grids were
521 placed nanowire side down on a glass slide, gold disks were sputtered with a 35 nm target
522 thickness at 1.5 x 10^{-2} Torr, and a process current of 30 mA. Grids were glow discharged
523 with air at 12mA for 80 secs using the internal Chameleon glow discharger. The grids
524 were plunged at 160 to 180 milliseconds. All images were acquired using a Titan Krios
525 microscope (FEI) operated at 300KeV with a Gatan K3 direct electron detector (Gatan).
526 Images were automatically acquired using Leginon (Suloway et al., 2005) using collection
527 parameters as shown in Table S1. This dataset was processed in cryoSPARC (Figure
528 S2). Briefly, templates were generated from our full-length ACE structure described above
529 using vitrobot-prepared grids. Micrographs with a max CTF value worse than 4Å were
530 removed from the dataset, leaving ~12,000 micrographs for template picking, which
531 yielded 10.7 million particles. The particle set was trimmed to ~2.8 million based on quality
532 metrics and run through 2 rounds of 2D classification, reducing the particle number to
533 ~660,000. 2D classes were dominated by 4 domain views, and yielded a much greater
534 diversity of views, indicating that Chameleon preparation produced a dramatic
535 improvement in particle quality. Initial 3D homogeneous refinement reached 3.6 Å,
536 matching the previous final structure. Four maps from 3D classes that contains all four
537 catalytic domains of ACE, one from particles derived from grids prepared by using vitrobot
538 and three from those prepared by using Chameleon, were used for structure building
539 using Chimera and Coot and the structure was refined using Phenix real space
540 refinement. Structural analysis was performed using PYMOL and Chimera.

541 **Heterogeneity analysis**: All heterogeneity analysis was performed on the full final
542 particle set, encompassing all of the NCCAT structures. Initially, cryoSPARC 3DVA was
543 performed on both the NCCAT- and UChicago-collected datasets and results were found
544 to be consistent, so the NCCAT-collected dataset was used for further analysis, given its
545 higher particle number and quality. Input particle poses for each method of heterogeneity

546 analysis were derived from the same C1 refinement job in cryoSPARC, which reached
547 2.88 Å. 3DVA was used to solve the top 5 modes of variance with a filter resolution of 6
548 Å. Particles were downsampled ~3x to a box size of 128 pixels in cryoDRGN to speed up
549 processing. The same downsampled particle set was used for both cryoDRGN and
550 RECOVAR. CryoDRGN was run with default parameters and the analysis was performed
551 on the top 5 principal components for direct comparison to cryoSPARC 3DVA. RECOVAR
552 pipeline.py was initially run on the full sACE structure. Reconstructions representative of
553 kmeans cluster centers revealed the dominant source of structural variability to be the
554 open-close transition in sACE-N. As a result, RECOVAR was run again with a focus mask
555 on sACE-N/N and a zdim=4. Conformational density was estimated with a 2-dimensional
556 PCA, and an index value of 3 was chosen for further analysis. The points in latent space
557 representing the top 12 stable conformational states were estimated from the top 20% of
558 particles and representative volumes were generated. The generated states populated
559 four clusters and the 12 states were simplified to 4 distinct conformations where sACE-
560 N/N adopted the open-open (OO), open-closed (OC), closed-open (CO), and closed-
561 closed (CC) states (Figure 5C). We then generated a trajectory through the latent space
562 using the OO and CC representative volumes as endpoints (Movie S7).

563 **All-atom MD simulations and analysis**: The sACE-3.65 structure was used to initiate
564 all MD simulations. For the glycosylated sACE simulations, N-linked glycans were built
565 onto all 12 known N-linked glycosylation sites (residues 38, 54, 74, 111, 146, 318, 445,
566 509, 677, 695, 714, 760) with the complex glycan BGLC-BGLC-BMAN-AMAN-BGLC-
567 ANE5-AMAN-BGLC-BGAL-ANE5-AFUC using CHARMM-GUI (Lee *et al*, 2016).
568 Simulations were prepared in QwikMD or CHARMM-GUI and run at pH 7, 150 mM NaCl,
569 310 K, 1 atm with periodic boundary conditions in NAMD3.0 using the University of
570 Chicago Beagle3 partition (Phillips *et al*, 2020). Explicit solvent was described with the
571 TIP3P model (Jorgensen *et al*, 1983). Data was analyzed in VMD 1.9.4 (Humphrey *et al*,
572 1996).

Figure + figure legends:

Figure 1: CryoEM analysis of human ACE dimer. (A) Diagram for the key features of domain on primary sequence of human ACE. To avoid confusion existing in the numbering of ACE structures, we number ACE based on Uniprot P12821-1. D1a and D3a domains, also called "lid" encompasses residues 31-127 and aa 645-725, respectively. D1b and D3b domains each have two discrete segments; residues 292-465 and 525-603 for D1b and residues 897-1060 and 1120-1200 for D3b. D2 encompasses three discrete segments, residues 128-291, 466-524, and 604-644 while D4 domain encompasses residues 726-896, 1061-1119, and 1201-1231. sp = signal peptide. asterisk = zinc binding motif. The construct used in this study comprises residues 1-1231, which we refer to as the soluble region of ACE (sACE). Colored by sub-domain: D1a cyan, D1b aqua, D2 pink, D3a light blue, D3b green, D4 magenta. (B) 2D classification of human sACE particles from grids made by vitrobot and Chameleon. Clear four domain classes visible in the Chameleon-derived classification are boxed in red, similar views are lacking in the vitrobot dataset. (C) Full-length sACE 3D volumes, colored by sub-domain as in (A). Glycan density is shown in gray. See Figure S2 for vitrobot-prepared data processing details, Figure S3 for Chameleon-prepared data processing details and Table S1 for data refinement statistics.

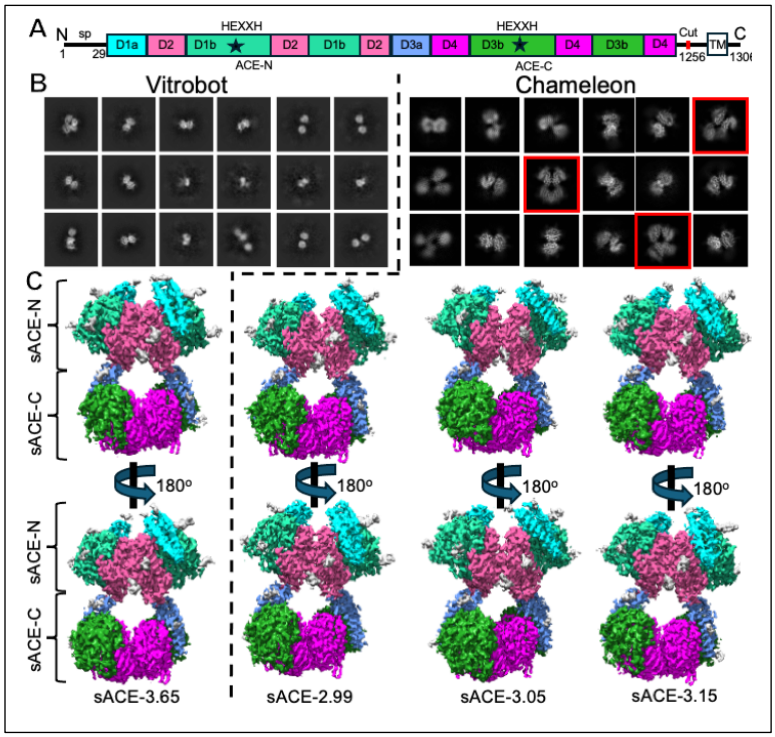

Figure 2: Overall structure of human ACE. (A) Overlay comparing sACE-N states highlighting the structure differences between the closed (C), intermediate (I), and open (O) states. (B) Overlay comparing sACE-C states highlighting the structure differences between the closed (C), and intermediate (I) states. We define the state based on the distance between the edge of the D2/4 domain bordering the catalytic cleft (residues 150-155 or 750-755) and the tip of the D1/3a region (residues 70-80 or 676-686): closed <15 Å, intermediate >15 Å and <19 Å, open >19 Å. (C) Overall dimer comparisons. (D) Table of openness measurements for each domain per structure.

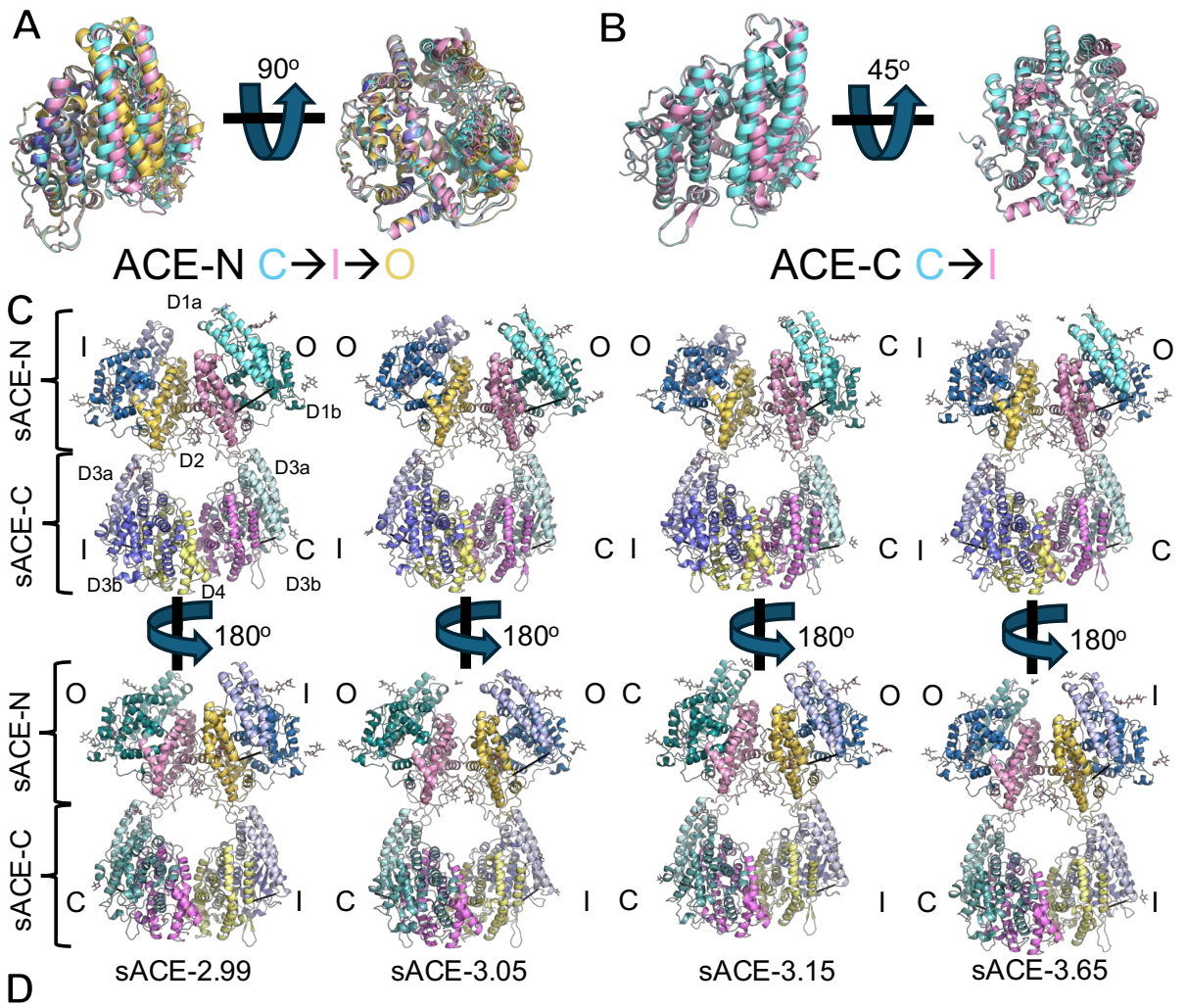

D

Opening distance (Å)	sACE-2.99		sACE-3.05		sACE-3.15		sACE-3.65	
	Chain A	Chain B	Chain A	Chain B	Chain A	Chain B	Chain A	Chain B
ACE-N	23.4 (O)	17.7 (I)	22.5 (O)	22.1 (O)	14.1 (C)	20.2 (O)	20.6 (O)	16.2 (I)
ACE-C	14.4 (C)	18.0 (I)	17.9 (I)	13.9 (C)	13.7 (C)	17.0 (I)	14.4 (C)	15.9(I)

Figure 3: sACE dimerization interfaces. (A) Overlay comparing sACE-N/N interface (blue) and sACE-C/C (yellow) interfaces. Interfaces adopt the same secondary structure but interacting residues vary between them. (B) Residue-specific interactions at the sACE-N/N interface, see text for details. (C) Unsharpened Coulomb potential density map (cyan) showing density corresponding to glycan-glycan interaction from N111 as part of sACE-N/N interface. Sharpened map is shown in magenta for reference. (D) Residue-specific interactions in the sACE-C/C interface, see text for details.

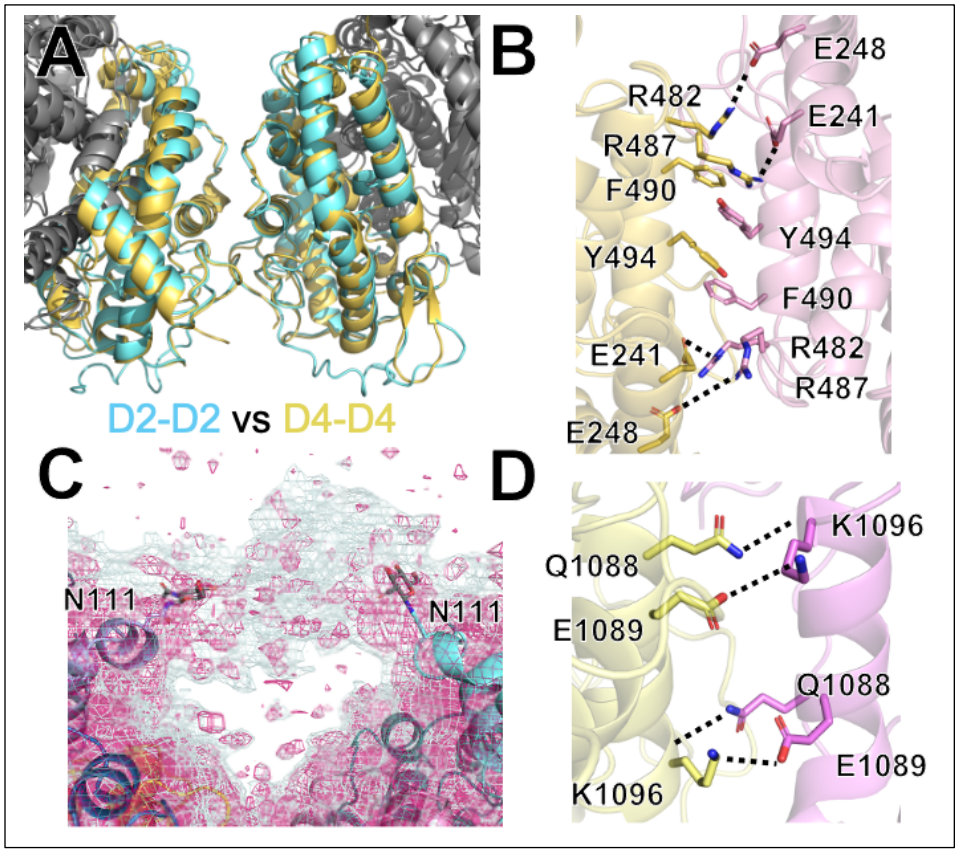

Figure 4: Structural mechanism of the sACE open/close transition. (A) sACE-N overlay comparing the open (colored in left panel, transparent gray in right panel) and closed (transparent gray in left panel, colored in right panel) states in detail. The open state is stabilized by interaction between residues in the D1a (cyan) and D2 (pink) regions that, notably K102-D218. In the closed state, the K102-D218 interaction is broken. (B) Overlay of the sACE-N open (cyan) and closed (pink) states showing the range of motion. The D1a region rotates about a fulcrum region described in (A), while the D1b region moves as a rigid body. (C) Overlay of sACE-C closed (light blue) and intermediate (yellow) states. Unlike sACE-N, the “top” of the D3a region is constrained by its connection to sACE-N

618 and largely immobile. The primary source of opening is only the motion of the D3a tip. We
619 did not observe any open state structures of sACE-C, suggesting a smaller range of
620 motion relative to sACE-N. (D) Comparison of the hydrophobic “latch” region formed in
621 the closed state between residues of the D1/3a, D1/3b, and D2/D4 domains. V753 in
622 sACE-C has been replaced by T153 in sACE-N, suggesting that the closed state in sACE-
623 N may be less stabilized than the sACE-C closed state. (E) Example all-atom MD
624 simulation tracking the openness of one sACE-N region (black line) and this distance
625 between K102 and D218 (red line). These residues form a salt bridge early in the
626 simulation when sACE-N is open (left inset) but the interaction breaks as sACE-N
627 transitions to the closed state (right inset). Distance measurements for MD simulations
628 were consistently greater than distance values in our static structures and cannot be
629 directly compared to Figure 2.

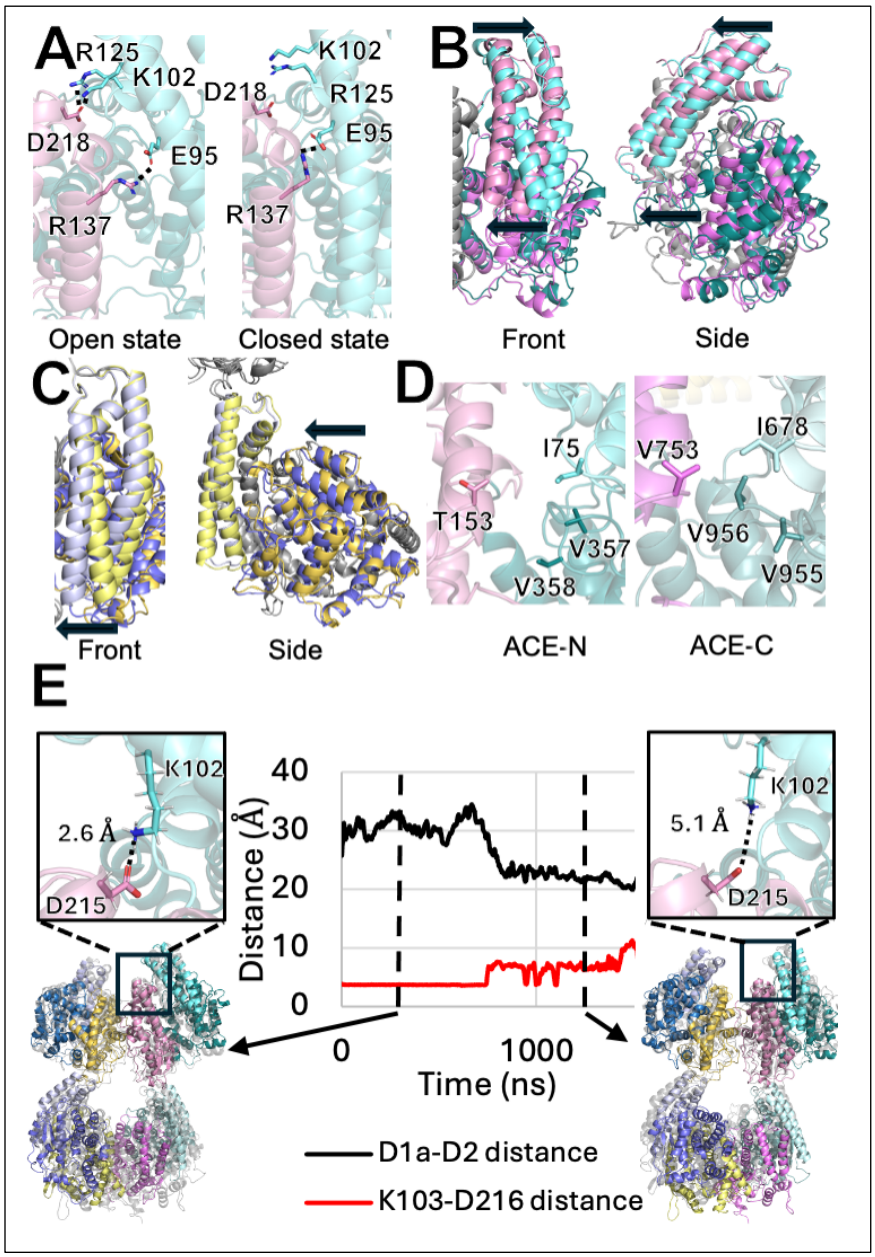

Figure 5: CryoEM heterogeneity analysis. (A) Visualization of the structural changes revealed by cryoSPARC 3DVA trajectories calculated along two principal components (PCs) of structural variance. Starting states are showing in cyan, ending states in gray. PC 0 reveals a large, inter-domain bending motion accompanied by the open/close transition in sACE-C. PC 1 and the remaining PCs are dominated by the open/close transition of individual regions. See Table S3, and Movie S7 for additional details. (B) Visualization of the structural changes revealed by the cryoDRGN trajectories calculated along two PCs of structural variance. Starting states are shown in cyan, ending states in gray. PCs are dominated by the open/close transition of individual regions. See Table S3, and Movie S8 for additional details. (C) Analysis in RECOVAR with a focus mask on

sACE-N/N reveals that particles adopt roughly four clusters within the latent space (heat map of particle density) corresponding to the open-open (OO, white square), open-closed (OC, white dot), closed-open (CO, white dot) and closed-closed (CC, white star) states of sACE-N/N. A trajectory estimating the path through latent space corresponding to the structural transition from sACE-N/N CC state to the OO state (blue points) suggests that individual sACE regions transition at different rates. See Movie S9 for trajectory. (D) Focused 3D classification was performed in cryoSPARC to explore evidence of coordinated motion between sACE-N regions. 3D classification focusing on one sACE-N region revealed 2 roughly equal classes of particles: open and closed. Subsequent 3D classification focused on the other sACE-N region again revealed 2 roughly equal classes, suggesting the lack of coordinated motion between sACE-N regions in the absence of substrate.

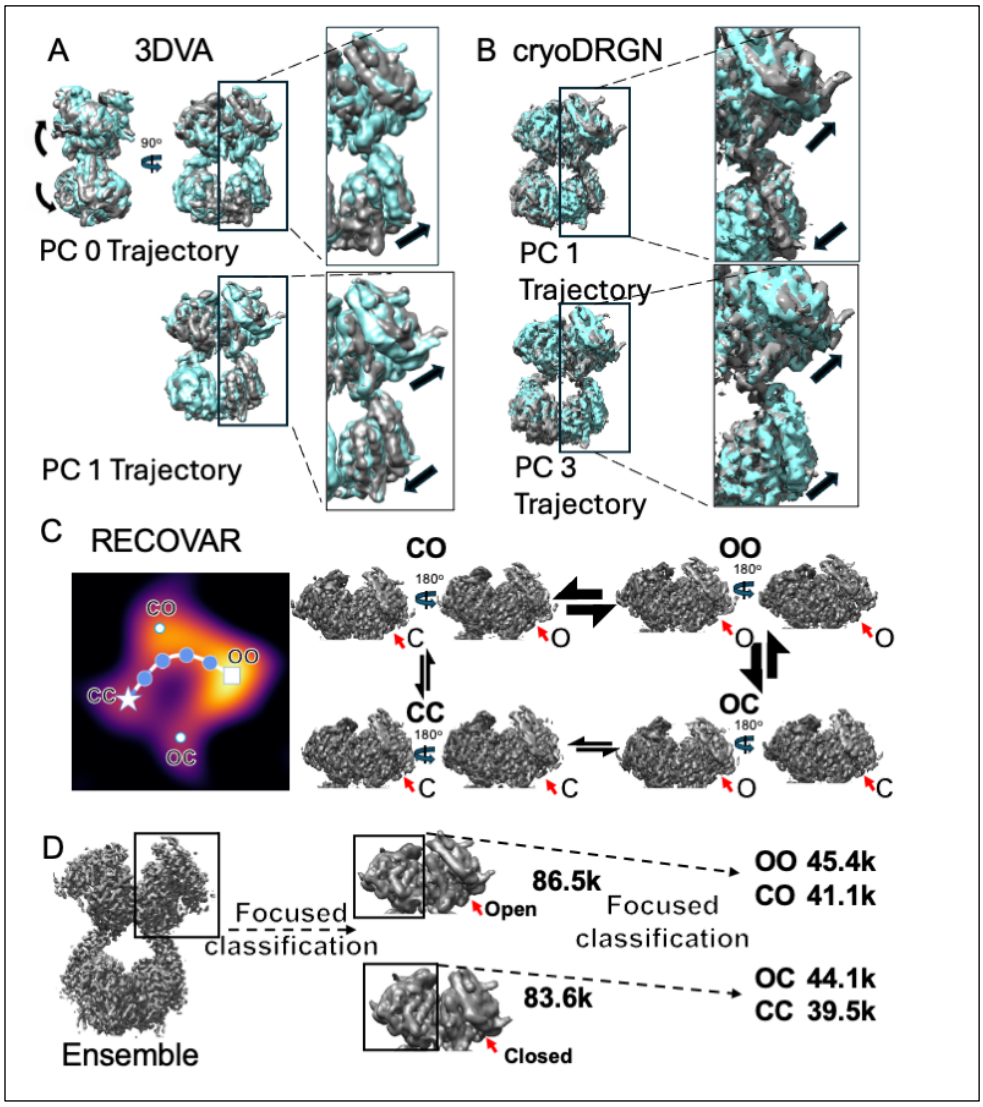

Data availability:

Unprocessed micrographs, particle stacks, and associated pose/CTF information have been deposited to EMPIAR under the accession numbers: EMPIAR-12181 (Vitrobot-prepared grids) and EMPIAR-12484 (Chameleon-prepared grids)

EM structures and maps have been deposited to the EMDB and PDB, respectively, under the following accession numbers:

sACE-2.99: 9D5S and EMD-46581

sACE-3.05: 9D5M and EMD-46579

sACE-3.15: 9D55 and EMD-46574

sACE-3.65: 9CLX and EMD-45733

References:

Acharya KR, Gregory KS, Sturrock ED (2024) Advances in the structural basis for angiotensin-1 converting enzyme (ACE) inhibitors. *Bioscience Rep* 44

Baudin B, Alves N, Pilon A, Beneteau-Burnat B, Giboudeau J (1997) Structural and biological roles of glycosylations in pulmonary angiotensin I-converting enzyme. *Glycobiology* 7: 565-570

Bernstein KE, Khan Z, Giani JF, Cao DY, Bernstein EA, Shen XZ (2018) Angiotensin-converting enzyme in innate and adaptive immunity. *Nat Rev Nephrol* 14: 325-336

Bernstein KE, Koronyo Y, Salumbides BC, Sheyn J, Pelissier L, Lopes DHJ, Shah KH, Bernstein EA, Fuchs DT, Yu JJY *et al* (2014) Angiotensin-converting enzyme overexpression in myelomonocytes prevents Alzheimer's-like cognitive decline. *J Clin Invest* 124: 1000-1012

Bernstein KE, Ong FS, Blackwell WLB, Shah KH, Giani JF, Gonzalez-Villalobos RA, Shen XZ, Fuchs S (2013) A Modern Understanding of the Traditional and Nontraditional Biological Functions of Angiotensin-Converting Enzyme. *Pharmacol Rev* 65: 1-46

Binevski PV, Sizova EA, Pozdnev VF, Kost OA (2003) Evidence for the negative cooperativity of the two active sites within bovine somatic angiotensin-converting enzyme. *Febs Lett* 550: 84-88

Chen GF, Xu TH, Yan Y, Zhou YR, Jiang Y, Melcher K, Xu HE (2017) Amyloid beta: structure, biology and structure-based therapeutic development. *Acta Pharmacol Sin* 38: 1205-1235

Corradi HR, Schwager SLU, Nchinda AT, Sturrock ED, Acharya KR (2006) Crystal structure of the N domain of human somatic angiotensin I-converting enzyme provides a structural basis for domain-specific inhibitor design. *Journal of Molecular Biology* 357: 964-974

Cozier GE, Lubbe L, Sturrock ED, Acharya KR (2021) Angiotensin-converting enzyme open for business: structural insights into the subdomain dynamics. *FEBS J* 288: 2238-2256

Danziger R, Fuchs DT, Koronyo Y, Rentsendorj A, Sheyn J, Hayden EY, Teplow DB, Black KL, Fuchs S, Bernstein KE *et al* (2023) The effects of enhancing angiotensin converting enzyme in myelomonocytes on ameliorating Alzheimer's-related disease and preserving cognition. *Front Physiol* 14: 1179315

Darrow MC, Moore JP, Walker RJ, Doering K, King RS (2019) Chameleon: Next Generation Sample Preparation for CryoEM based on Spotiton. *Microscopy and Microanalysis* 25: 994-995

English WR, Corvol P, Murphy G (2012) LPS activates ADAM9 dependent shedding of ACE from endothelial cells. *Biochem Bioph Res Co* 421: 70-75

Erdos EG, Tan F, Skidgel RA (2010) Angiotensin I-converting enzyme inhibitors are allosteric enhancers of kinin B1 and B2 receptor function. *Hypertension* 55: 214-220

Glaeser RM (2018) Proteins, interfaces, and cryo-EM grids. *Curr Opin Colloid In* 34: 1-8

Gomis-Ruth FX (2008) Structure and Mechanism of Metallocarboxypeptidases. *Critical Reviews in Biochemistry and Molecular Biology* 43: 319-345

Gouveia F, Camins A, Ettcheto M, Bicker J, Falcao A, Cruz MT, Fortuna A (2022) Targeting brain Renin-Angiotensin System for the prevention and treatment of Alzheimer's disease: Past, present and future. *Ageing Res Rev* 77

Hampel H, Hardy J, Blennow K, Chen C, Perry G, Kim SH, Villemagne VL, Aisen P, Vendruscolo M, Iwatsubo T *et al* (2021) The Amyloid-β Pathway in Alzheimer's Disease. *Mol Psychiatr* 26: 5481-5503

Hemming ML, Selkoe DJ (2005) Amyloid beta-protein is degraded by cellular angiotensin-converting enzyme (ACE) and elevated by an ACE inhibitor. *J Biol Chem* 280: 37644-37650

Herman LL, Padala SA, Ahmed I, Bashir K (2024) Angiotensin-Converting Enzyme Inhibitors (ACEI). In: *StatPearls*, Treasure Island (FL) ineligible companies. Disclosure: Sandeep Padala declares no relevant financial relationships with ineligible companies. Disclosure: Intisar Ahmed declares no relevant financial relationships with ineligible companies. Disclosure: Khalid Bashir declares no relevant financial relationships with ineligible companies.

Humphrey W, Dalke A, Schulten K (1996) VMD: visual molecular dynamics. *J Mol Graph* 14: 33-38, 27-38

Jorgensen WL, Chandrasekhar J, Madura JD, Impey RW, Klein ML (1983) Comparison of Simple Potential Functions for Simulating Liquid Water. *J Chem Phys* 79: 926-935

Kost OA, Bovin NV, Chemodanova EE, Nasonov VV, Orth TA (2000) New feature of angiotensin-converting enzyme: carbohydrate-recognizing domain. *J Mol Recognit* 13: 360-369

Lee J, Cheng X, Swails JM, Yeom MS, Eastman PK, Lemkul JA, Wei S, Buckner J, Jeong JC, Qi YF *et al* (2016) CHARMM-GUI Input Generator for NAMD, GROMACS, AMBER, OpenMM, and CHARMM/OpenMM Simulations Using the CHARMM36 Additive Force Field. *J Chem Theory Comput* 12: 405-413

Liang WG, Mancl JM, Zhao M, Tang WJ (2021) Structural analysis of Mycobacterium tuberculosis M13 metalloprotease Zmp1 open states. *Structure* 29: 709-720

Liang WG, Wijaya J, Wei H, Noble AJ, Mancl JM, Mo S, Lee D, Lin King JV, Pan M, Liu C *et al* (2022) Structural basis for the mechanisms of human presequence protease conformational switch and substrate recognition. *Nat Commun* 13: 1833

Lubbe L, Cozier GE, Oosthuizen D, Acharya KR, Sturrock ED (2020) ACE2 and ACE: structure-based insights into mechanism, regulation and receptor recognition by SARS-CoV. *Clin Sci* 134: 2851-2871

Lubbe L, Sewell BT, Woodward JD, Sturrock ED (2022) Cryo-EM reveals mechanisms of angiotensin I-converting enzyme allostery and dimerization. *EMBO J* 41: e110550

Malito E, Hulse RE, Tang WJ (2008) Amyloid β-degrading cryptidases: insulin degrading enzyme, presequence peptidase, and neprilysin. *Cell Mol Life Sci* 65: 2574-2585

Masuyer G, Schwager SLU, Sturrock ED, Isaac RE, Acharya KR (2012) Molecular recognition and regulation of human angiotensin-I converting enzyme (ACE) activity by natural inhibitory peptides. *Sci Rep* 2: 717

Natesh R, Schwager SLU, Sturrock ED, Acharya KR (2003) Crystal structure of the human angiotensin-converting enzyme-lisinopril complex. *Nature* 421: 551-554

Noble AJ, Wei H, Dandey VP, Zhang Z, Tan YZ, Potter CS, Carragher B (2018) Reducing effects of particle adsorption to the air-water interface in cryo-EM. *Nat Methods* 15: 793-795

O'Neill HG, Redelinghuys P, Schwager SLU, Sturrock ED (2008) The role of glycosylation and domain interactions in the thermal stability of human angiotensin-converting enzyme. *Biol Chem* 389: 1153-1161

Orth T, Voronov S, Binevski P, Saenger W, Kost O (1998) Glycosylation of bovine pulmonary angiotensin-converting enzyme modulates its catalytic properties. *Febs Lett* 431: 255-258

Phan TTV, Heo SY, Jung WK, Yi M (2020) Spontaneous Hinge-Bending Motions of Angiotensin I Converting Enzyme: Role in Activation and Inhibition. *Molecules* 25: 1288

Phillips JC, Hardy DJ, Maia JDC, Stone JE, Ribeiro JV, Bernardi RC, Buch R, Fiorin G, Hénin J, Jiang W *et al* (2020) Scalable molecular dynamics on CPU and GPU architectures with NAMD. *J Chem Phys* 153

Punjani A, Fleet DJ (2021) 3D variability analysis: Resolving continuous flexibility and discrete heterogeneity from single particle cryo-EM. *J Struct Biol* 213

Punjani A, Fleet DJ (2023) 3DFlex: determining structure and motion of flexible proteins from cryo-EM. *Nature Methods* 20: 860-+

Punjani A, Rubinstein JL, Fleet DJ, Brubaker MA (2017) cryoSPARC: algorithms for rapid unsupervised cryo-EM structure determination. *Nat Methods* 14: 290-296

Qiu WQ, Mwamburi M, Besser LM, Zhu HH, Li HJ, Wallack M, Phillips L, Qiao LY, Budson AE, Stern R *et al* (2013) Angiotensin Converting Enzyme Inhibitors and the Reduced Risk of Alzheimer's Disease in the Absence of Apolipoprotein E4 Allele. *J Alzheimers Dis* 37: 421-428

Rice GI, Thomas DA, Grant PJ, Turner AJ, Hooper NM (2004) Evaluation of angiotensin-converting enzyme (ACE), its homologue ACE2 and neprilysin in angiotensin peptide metabolism. *Biochem J* 383: 45-51

Riordan JF (2003) Angiotensin-I-converting enzyme and its relatives. *Genome Biol* 4: 225

762 Sadhukhan R, Sen I (1996) Different glycosylation requirements for the synthesis of enzymatically
763 active angiotensin-converting enzyme in mammalian cells and yeast. *J Biol Chem* 271: 6429-6434
764 Semis M, Gugiu GB, Bernstein EA, Bernstein KE, Kalkum M (2019) The Plethora of Angiotensin-
765 Converting Enzyme-Processed Peptides in Mouse Plasma. *Anal Chem* 91: 6440-6453
766 Skirgello OE, Binevski PV, Pozdnev VF, Kost OA (2005) Kinetic probes for inter-domain co-operation in
767 human somatic angiotensin-converting enzyme. *Biochem J* 391: 641-647
768 Tang WJ (2016) Targeting Insulin-Degrading Enzyme to Treat Type 2 Diabetes Mellitus. *Trends*
769 *Endocrinol Metab* 27: 24-34
770 Tang WS, Zhong ED, Hanson SM, Thiede EH, Cossio P (2023) Conformational heterogeneity and
771 probability distributions from single-particle cryo-electron microscopy. *Curr Opin Struc Biol* 81
772 Turner AJ, Hooper NM (2002) The angiotensin-converting enzyme gene family: genomics and
773 pharmacology. *Trends Pharmacol Sci* 23: 177-183
774 Wright JW, Kawas LH, Harding JW (2013) A Role for the Brain RAS in Alzheimer's and Parkinson's
775 Diseases. *Front Endocrinol (Lausanne)* 4: 158
776 Yu XC, Sturrock ED, Wu Z, Biemann K, Ehlers MR, Riordan JF (1997) Identification of N-linked
777 glycosylation sites in human testis angiotensin-converting enzyme and expression of an active
778 deglycosylated form. *J Biol Chem* 272: 3511-3519
779 Zhang Y, Chen H, Li R, Sterling K, Song W (2023) Amyloid beta-based therapy for Alzheimer's disease:
780 challenges, successes and future. *Signal Transduct Target Ther* 8: 248
781 Zhang ZN, Liang WGG, Bailey LJ, Tan YZ, Wei H, Wang A, Farcasanu M, Woods VA, McCord LA, Lee D
782 *et al* (2018) Ensemble cryoEM elucidates the mechanism of insulin capture and degradation by
783 human insulin degrading enzyme. *Elife* 7: e33572
784 Zheng WY, Tian EK, Liu Z, Zhou CH, Yang P, Tian KY, Liao W, Li J, Ren CY (2022) Small molecule
785 angiotensin converting enzyme inhibitors: A medicinal chemistry perspective. *Front Pharmacol* 13
786 Zou K, Maeda T, Watanabe A, Liu JJ, Liu SY, Oba R, Satoh Y, Komano H, Michikawa M (2009) A beta 42-
787 to-A beta 40-and Angiotensin-converting Activities in Different Domains of Angiotensin-converting
788 Enzyme. *J Biol Chem* 284: 31914-31920

789

790